Connecting the escape fraction of Lyman-alpha and Lyman-continuum photons in star-forming galaxies at $z \simeq 4-5$

R. Begley^{1*}, F. Cullen¹, R. J. McLure¹, A. E. Shapley², J. S. Dunlop¹, A. C. Carnall¹, D. J. McLeod¹, C. T. Donnan¹, M. L. Hamadouche¹ and T. M. Stanton¹

Accepted XXXX. Received YYYY; in original form ZZZZ

ABSTRACT

We present a study of the connection between the escape fraction of Lyman-alpha (Ly α) and Lyman-continuum (LyC) photons within a sample of N=152 star-forming galaxies selected from the VANDELS survey at $3.85 \le z_{\rm spec} \le 4.95$ ($\langle z_{\rm spec} \rangle = 4.36$). By combining measurements of H α equivalent width ($W_{\lambda}({\rm H}\alpha)$) derived from broad-band photometry with measurements of Ly α equivalent width ($W_{\lambda}({\rm Ly}\alpha)$) from the VANDELS spectra, we individually estimate $f_{\rm esc}^{\rm Ly}$ for our full sample. In agreement with previous studies, we find a positive correlation between $W_{\lambda}({\rm Ly}\alpha)$ and $f_{\rm esc}^{\rm Ly}$ increasing from $f_{\rm esc}^{\rm Ly} = 0.04$ at $W_{\lambda}({\rm Ly}\alpha) = 10$ Å to $f_{\rm esc}^{\rm Ly} = 0.1$ at $W_{\lambda}({\rm Ly}\alpha) = 25$ Å. For the first time at z = 4-5, we investigate the relationship between $f_{\rm esc}^{\rm Ly}$ and $f_{\rm esc}^{\rm Ly}$ using $f_{\rm esc}^{\rm Ly}$ estimates derived using the equivalent widths of low-ionization, far-UV absorption lines in composite VANDELS spectra. Our results indicate that $f_{\rm esc}^{\rm Ly}$ rises monotonically with $f_{\rm esc}^{\rm Ly}$, following a relation of the form $f_{\rm esc}^{\rm Ly} = 0.15 f_{\rm esc}^{\rm Ly}$. Based on composite spectra of sub-samples with approximately constant $W_{\lambda}({\rm Ly}\alpha)$, but widely different $f_{\rm esc}^{\rm Ly} = 0.15 f_{\rm esc}^{\rm Ly} = 0.15 f_{\rm$

Key words: galaxies: high-redshift – galaxies: fundamental parameters – intergalactic medium

1 INTRODUCTION

The formation of the first stars and the growth of galaxy progenitors in the early Universe signalled the beginning of the Epoch of reionization (EOR), during which the fully neutral Hydrogen gas in the intergalactic medium (IGM) became completely ionized (e.g., Robertson et al. 2015). Although it is generally acknowledged that reionization was completed between $z \sim 5-6$, based primarily on measurements of the Ly α forest from distant quasars (e.g., Fan et al. 2006; McGreer et al. 2015; Goto et al. 2021), key details of the process of reionization and the nature of the sources responsible remain a matter of debate (e.g., Mason et al. 2019; Naidu et al. 2020).

One fundamental reason for the continued debate is that the progress of reionization is intimately linked to the physical properties of the sources that are responsible for it, as well as their location within the large-scale structure of the Universe (Robertson 2021). It is now widely accepted that active galactic nuclei are simply too rare at high redshift to contribute significantly to reionization (e.g., Matsuoka et al. 2023) and that the dominant contribution to the ionizing photon budget must come from star-forming galaxies (SFGs) (e.g., Robertson et al. 2015; Chary et al. 2016; Iwata et al. 2022).

A key component needed to quantify the ionizing photon budget

is the abundance of star-forming galaxies during the EOR, most commonly parameterised through the UV luminosity density ($\rho_{\rm UV}$), that is now being established with increasing accuracy out to $z \simeq 12$ by JWST (e.g., Donnan et al. 2022; Finkelstein et al. 2022; Harikane et al. 2022). The latest JWST results indicate that $\rho_{\rm UV}$ displays a smooth, steady decline through the EOR (e.g., Donnan et al. 2023; McLeod et al. 2023) indicating, in principle, the availability of more ionizing photons than some pre-JWST studies (e.g., Oesch et al. 2018; Ishigaki et al. 2018) had suggested.

Another essential element is the ionizing photon production efficiency $\xi_{\rm ion}$, a measure of the number of ionizing photons produced per unit UV luminosity of the star-forming galaxy population. Recent evidence has suggested that the faint, blue population of galaxies commonly found at z>6 (i.e. with UV spectral slope $\beta\lesssim -2.3$; Cullen et al. 2023) display $\log(\xi_{\rm ion})$ in the range $\sim 25.5-25.8$ (Stark et al. 2015; Bouwens et al. 2016), a factor of $\geq 2-3$ higher than canonically assumed in models of reionization (e.g., Bouwens et al. 2012; Finkelstein et al. 2012; Duncan & Conselice 2015).

Although the abundance of SFGs and the elevated values of $\xi_{\rm ion}$ at z>6 indicate that sufficient numbers of ionizing photons are being generated within the EOR, whether or not these Lyman-continuum (LyC) photons escape their source galaxies and ionize the IGM is ultimately determined by the escape fraction ($f_{\rm esc}^{\rm LyC}$).

¹Institute for Astronomy, University of Edinburgh, Royal Observatory, Edinburgh EH9 3HJ, UK

²Department of Physics & Astronomy, University of California, Los Angeles, 430 Portola Plaza, Los Angeles, CA 90095, USA

^{*} E-mail:rbeg@roe.ac.uk

Due to the near-total attenuation of UV photons below the Lyman break by the IGM at $z \ge 4$ (e.g., Steidel et al. 2018), direct observational constraints on $f_{\rm esc}^{\rm LyC}$ are only possible up to $z \simeq 3.8$. At the highest redshifts where such observations are possible, recent estimates from deep photometric and spectroscopic studies have typically constrained the average $f_{\rm esc}^{\rm LyC}$ to be $\simeq 5-10\%$ (e.g., Steidel et al. 2018; Pahl et al. 2021; Meštrić et al. 2021; Begley et al. 2022; Saldana-Lopez et al. 2022a). Generally, these studies have also found that the fainter, less-dust-obscured galaxies that are expected to be numerous during the EOR are more likely to display high $f_{\rm esc}^{\rm LyC}$. Promisingly, these trends are in accordance with the assumptions that are often made in reionization models (Robertson et al. 2010; Wise et al. 2014; Robertson et al. 2015; Finkelstein et al. 2019) where $\langle f_{\rm esc}^{\rm LyC} \rangle \geq$ 5% is typically required for reionization to be completed

In spite of these encouraging results, we still lack a comprehensive understanding of exactly how LyC photons escape galaxies. To this end, a number of studies have attempted to link $f_{\rm esc}^{\rm LyC}$ to nebular emission-line features, such as Mg II (Katz et al. 2022), C IV (Schaerer et al. 2022) and [O III] (e.g., Verhamme et al. 2015; Wang et al. 2019; Izotov et al. 2020; Nakajima et al. 2020), which are modulated by the same interstellar medium (ISM) and stellar-population properties that ultimately determine $f_{\rm esc}^{\rm LyC}$.

One of the most promising and closely investigated indicators is the Ly α emission line, with a number of studies showing that strong Ly α emission (i.e., identified by a high Ly α equivalent width, $W_{\lambda}(\text{Ly}\,\alpha)$) is an excellent indicator of high $f_{\text{esc}}^{\text{LyC}}$ (Marchi et al. 2018; Pahl et al. 2021; Begley et al. 2022). Furthermore, a clear correlation between $f_{\text{esc}}^{\text{Ly}\alpha}$ and $f_{\text{esc}}^{\text{Ly}C}$ has been found by Flury et al. (2022b), using galaxies at z = 0.2using galaxies at $z \approx 0.3$ selected from the Low Redshift Lyman Continuum Survey (LzLCS; Flury et al. 2022a); a finding consistent with simulation results (e.g, Dijkstra et al. 2016; Kimm et al. 2019).

This Ly α –LyC connection is expected given that $f_{\rm esc}^{\rm Ly}\alpha$ and $f_{\rm esc}^{\rm Ly}$ are both modulated by the geometry and nature of the gas in the vicinity of young star-forming regions (e.g., Shapley et al. 2003; Chisholm et al. 2018; Gazagnes et al. 2020; Maji et al. 2022). Furthermore, the characteristics of the young stellar populations themselves influence both LyC and Ly α photon production, with low-metallicity stellar populations having higher $\xi_{\rm ion}$ and therefore producing more LyC and Ly α photons for a given star-formation rate (e.g., Trainor et al. 2015; Erb et al. 2016; Trainor et al. 2016; Cullen et al. 2020).

The main escape path for ionizing photons is likely through channels of low-column-density, and/or high-ionization-state gas in the ISM, through which Ly α photons can also escape in significant quantities (e.g., Atek et al. 2008; Dijkstra et al. 2016; Jaskot et al. 2019). Gazagnes et al. (2020) presented strong observational evidence for LyC leakage via this mechanism, finding significant correlations between the presence of low H_I covering fractions and the observed LyC escape fraction. Similar correlations have been found in several other independent observational studies (e.g., Verhamme et al. 2017; Chisholm et al. 2018; Saldana-Lopez et al. 2022b).

This argument is further bolstered by the well-established links between Ly α and the ISM properties of galaxies. Shapley et al. (2003) showed that the observed range of $W_{\lambda}(Ly \alpha)$ in Lyman break galaxies at $z \sim 3$ is accounted for by variations in the covering fraction of neutral outflowing H I gas and dust (see also; Atek et al. 2008; Kornei et al. 2010; Berry et al. 2012; Reddy et al. 2016). More-recent literature studies have uncovered a relationship between $W_{\lambda}(\text{Ly }\alpha)$ and the covering fraction of neutral gas, as traced by the strength of low-ionization-state ISM absorption lines (Henry et al.

2015; Du et al. 2018; Steidel et al. 2018; Jaskot et al. 2019; Trainor et al. 2019).

In this study, we explore the connection between Ly α and LyC escape in galaxies only $\simeq 300$ Myr after reionization was completed, using a sample of galaxies in the range $3.85 \le z_{\rm spec} \le 4.95$ drawn from the VANDELS ESO public spectroscopic survey. We combine direct Ly α line measurements from the VANDELS spectra with H α luminosity constraints based on robust SED fitting, allowing us to individually estimate $f_{\rm esc}^{{\rm Ly}\alpha}$ for each galaxy. Using composite spectra formed from sub-samples of Ly α emitters, we then investigate how $f_{\rm esc}^{\rm LyC}$, as estimated from FUV LIS ISM line strengths, varies with $f_{\rm esc}^{\rm Ly}\alpha$ and $W_{\lambda}({\rm Ly}\,\alpha)$.

The structure of the paper is as follows. In Section 2 we describe the VANDELS spectral dataset, the associated photometric catalogues and our sample selection criteria. In Section 3 we describe the methodology used to derive the individual $f_{\rm esc}^{\rm Ly\alpha}$ measurements. In Section 4 we explore the $f_{\rm esc}^{\rm Ly\alpha} - W_{\lambda}({\rm Ly}\,\alpha)$ correlation, before presenting our constraints on $\langle f_{\rm esc}^{\rm Ly} \rangle$ and proceeding to constrain $f_{\rm esc}^{\rm LyC}$ from the strength of low-ionization-state absorption lines in composite VANDELS spectra. We provide a discussion of our main results in Section 5 and present our conclusions in Section 6. Throughout the paper we adopt the following cosmological parameters: $H_0 = 70 \,\mathrm{km \, s^{-1} Mpc^{-1}}$, $\Omega_{\rm m} = 0.3$, $\Omega_{\Lambda} = 0.7$ and all magnitudes are quoted in the AB system (Oke & Gunn 1983).

2 DATA AND SAMPLE SELECTION

Our sample of star-forming galaxies is drawn from the VANDELS ESO public spectroscopic survey final data release (DR4, Garilli et al. 2021). The VANDELS survey used the VIMOS spectrograph (Le Fèvre et al. 2003) installed on the ESO Very Large Telescope (VLT) to obtain ultra-deep spectra of 2087 galaxies at red-optical wavelengths $(4800 \text{ Å} < \lambda < 10000 \text{ Å})$ in the Chandra Deep Field South (CDFS) and UKIDSS Ultra Deep Survey (UDS) fields (McLure et al. 2018; Pentericci et al. 2018). The vast majority of VANDELS targets were main-sequence star-forming galaxies at $2.4 \le z \le 7.0$, for which the ultra-deep (20 – 80 hour integration) VIMOS spectra cover the rest-frame far-ultraviolet (FUV), enabling measurements of the Ly α line (e.g., Cullen et al. 2020). Full details of the survey design and target selection can be found in McLure et al. (2018).

All galaxies targeted in VANDELS benefit from deep, multiwavelength imaging data covering the observed wavelength range $0.38~\mu\mathrm{m} \lesssim \lambda_{\mathrm{obs}}~\lesssim~4.5~\mu\mathrm{m}$. Approximately half of the VANDELS sample lies within the CANDELS GOODS-S and UDS Hubble Space Telescope (HST) imaging footprint (Koekemoer et al. 2011; Grogin et al. 2011), for which we adopt the photometry from Guo et al. (2013) and Galametz et al. (2013), respectively. The other half of the sample lies outside the CANDELS footprint, but benefits from wider-area, primarily ground-based optical/nearIR imaging. For this study we adopt the updated VANDELS photometry catalogues described in Garilli et al. (2021) and publicly released as part of DR4. Crucially, in addition to optical/near-IR data, the full VANDELS sample benefits from deep, deconfused Spitzer IRAC photometry at 3.6 μ m and 4.5 μ m. As discussed below, it is the photometric excess at 3.6 μ m that provides our measurement of H α line flux, with the $4.5 \mu m$ photometry providing a long-wavelength (emission-line free) anchor for the SED fitting.

Our initial sample consists of all VANDELS galaxies in the redshift range $3.85 \le z_{\rm spec} \le 4.95$, within which the IRAC $3.6 \,\mu{\rm m}$ filter is contaminated by the H α emission line. In addition, to ensure the

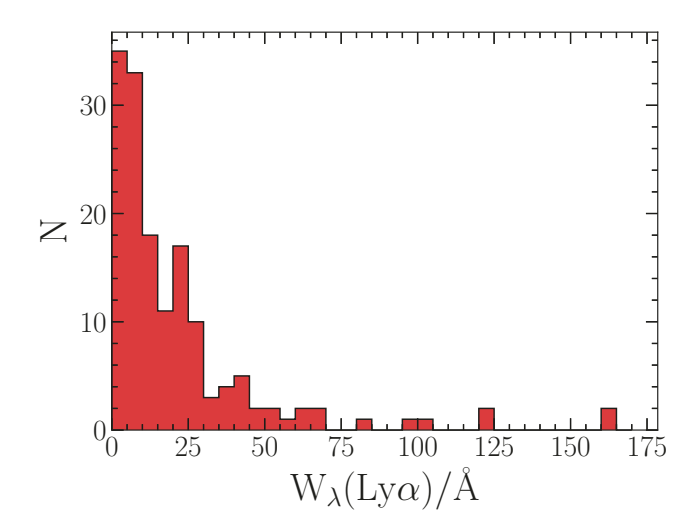


Figure 1. The distribution of rest-frame Ly α equivalent width for our final sample of N=152 star-forming galaxies at $3.85 \le z_{\rm spec} \le 4.95$ showing Ly α in emission. The median rest-frame equivalent width is $\langle W_{\lambda}({\rm Ly}\,\alpha)\rangle = 11.9\,{\rm \AA}$.

redshifts are robust, we restricted the sample to the N=263 galaxies in this redshift range with redshift quality flags of $z_{\rm flag}=3,4$ or 9, corresponding to a $\geq 95\%$ probability of being correct (Garilli et al. 2021). Finally, in order to measure Ly α escape fractions, we restricted the sample to galaxies which displayed Ly α in emission (i.e., an equivalent width > 0 Å; see below), resulting in a sample of N=152 galaxies with a median redshift of $\langle z \rangle = 4.36$.

3 EMISSION LINE FLUX MEASUREMENTS

Our principal aim is to determine Ly α escape fractions for the galaxies in our sample. To do this we combine measurements of the *observed* Ly α flux (measured directly from the VANDELS spectra) with estimates of the *intrinsic* flux derived from the observed H α flux (measured using the IRAC 3.6 μ m flux excess). In this section, we describe each stage in the process of deriving our Ly α escape fraction measurements for our sample of $3.85 \le z_{\rm spec} \le 4.95$ galaxies.

3.1 Observed Ly α fluxes and equivalent widths

Observed Ly α fluxes and rest-frame equivalent widths, $W_{\lambda}(\text{Ly}\,\alpha)$, are measured from the VANDELS spectra following the method described by Kornei et al. (2010) and adopted in our previous analysis of the correlation between $W_{\lambda}(\text{Ly}\,\alpha)$ and stellar metallicity (Cullen et al. 2020). Briefly, the line flux is measured by integrating the spectrum around the peak of the Ly α emission line, between limits defined as the wavelengths where the spectrum intersects the 'red' and 'blue' continuum levels, defined as the median flux between $1120\text{\AA} \leq \lambda_{\text{rest}} \leq 1180\text{\AA}\ (c_{\text{blue}})$ and $1228\text{\AA} \leq \lambda_{\text{rest}} \leq 1255\text{\AA}\ (c_{\text{red}})$, respectively¹. The rest-frame equivalent width is then simply obtained by dividing the integrated Ly α line flux by $c_{\text{red}}(1+z)$.

For each galaxy, the above process is repeated 500 times, each time perturbing the galaxy spectrum on a pixel-by-pixel basis by

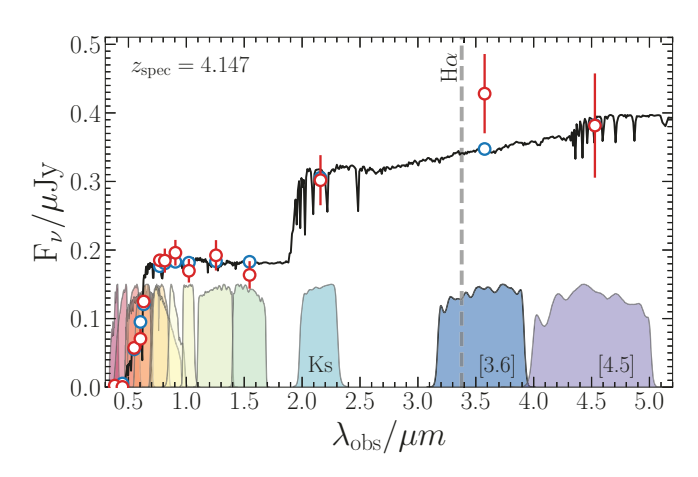


Figure 2. The best-fitting SED model from FAST++ for an example galaxy at $z_{\rm spec} = 4.147$. SED fits to the observed fluxes (red points) excluding the IRAC 3.6 μ m filter which is contaminated by H α emission (dashed grey line) allows the excess between the observed and predicted 3.6 μ m flux (blue points) to be measured. In this example, the flux excess is Δ mag = $-0.22^{+0.16}_{-0.13}$, corresponding to W_A (H α)= 250 ± 170 Å. The normalised transmission profiles for the multi-wavelength photometry available for this galaxy are shown in the lower half of the panel.

its corresponding error value. From the resulting distribution, the median and scaled median absolute deviation ($\sigma_{\rm MAD} \simeq 1.4826 \times {\rm MAD}$) are calculated and adopted as the final rest-frame $W_{\lambda}({\rm Ly}\,\alpha)$ and uncertainty. The equivalent width distribution of our final sample of N=152 galaxies showing Ly α emission is shown in Fig. 1.

3.2 Observed H α fluxes and equivalent widths

To estimate the *intrinsic* Ly α flux we first obtain an estimate of the observed H α flux and nebular dust attenuation (see also; Section 3.3) from SED fitting the available multi-wavelength photometry. When fitting the photometry we exclude the IRAC 3.6 μ m filter containing the H α line, which enables a robust estimate of the $W_{\lambda}(H\alpha)$ and H α line flux, via the well-known photometric excess technique (Fig. 2; e.g., Stark et al. 2013; Bouwens et al. 2016; Mármol-Queraltó et al. 2016; Smit et al. 2016). Below we give details of the stellar population modelling and our method for deriving $W_{\lambda}(H\alpha)$.

3.2.1 Stellar population modelling

In this analysis we use the FAST++ code (Kriek et al. 2009; Schreiber et al. 2018) to perform SED fitting for each galaxy, using Bruzual & Charlot (2003) stellar population synthesis models with a Chabrier (2003) IMF and a metallicity range of $0.2-0.4\times Z_{\odot}$. We assume a constant star-formation history, with the age allowed to vary within the range $6.7 \le \log(t/yr) \le 10.0$ in steps of $\Delta(\log(t/yr)) = 0.2$. We adopt the Calzetti et al. (2000) dust attenuation law and allow the absolute attenuation A_V to vary within the range $0.0 \le A_V \le 4.0$. All photometric data points are included in the SED fitting, except for the IRAC $3.6~\mu m$ filter, and we do not include nebular emission in the SED fits (see Fig. 2 for an example). Our final sample has a median stellar mass of $\langle \log(M_*/M_{\odot}) \rangle = 9.08$ and a median star-formation rate of $\langle \log(SFR/M_{\odot}yr^{-1}) \rangle = 1.12$, fully consistent with being located on the star-forming main sequence at $z \simeq 4-5$.

¹ For three objects no continuum was detected in the spectra and continuum levels were estimated from the best-fitting SED model (Section 3.2.1).

3.2.2 $H\alpha$ equivalent widths

For each galaxy in our sample the H α equivalent width is estimated by comparing the observed IRAC 3.6 μ m flux to the stellar population model prediction (see Fig. 2). For each galaxy we determine

$$\Delta[3.6\mu\text{m}] = m_{\text{obs}}^{3.6\mu\text{m}} - m_{\text{mod}}^{3.6\mu\text{m}}, \tag{1}$$

where $m_{obs}^{3.6\mu m}$ and $m_{mod}^{3.6\mu m}$ are the observed and model apparent magnitudes in the IRAC $3.6\mu m$ filter, respectively. The resulting distribution of $\Delta[3.6\mu m]$ is shown in Fig. 3. The distribution shows a clear systematic shift from $\Delta[3.6\mu m]=0$ towards negative values (median $\Delta[3.6\mu m]=-0.31$), signifying the presence of H α emission in the majority of our sample. Based on the IRAC $3.6\,\mu m$ excess, we estimate the rest-frame H α equivalent width using

$$W_{\lambda}({\rm H}\,\alpha) = f_{{\rm H}\,\alpha} \times \frac{W_{\rm eff}^{3.6\mu m}}{1+z_{\rm spec}} \times \left(10^{-0.4 \times \Delta[3.6\mu m]} - 1\right),$$
 (2)

where $W_{\rm eff}^{3.6\mu{\rm m}}=6844~{\rm \AA}$ is the effective width of the 3.6 $\mu{\rm m}$ filter and $f_{\rm H\,\alpha}$ is the fraction of the total contaminating line flux attributed to the H α line alone (i.e. excluding [N II] $\lambda 6584~{\rm \AA}$ and [S II] $\lambda \lambda 6717,6731~{\rm \AA}$). The value of $f_{\rm H\,\alpha}$ is often cited to be in the range $f_{\rm H\,\alpha}\simeq 0.71-0.9$ (e.g., Shim et al. 2011; Stark et al. 2013; Mármol-Queraltó et al. 2016; Smit et al. 2016). In this analysis, we use a fiducial conversion of factor of $f_{\rm H\,\alpha}=0.84$, following Smit et al. (2016).

The median value of $\Delta[3.6\mu\mathrm{m}] = -0.31$ corresponds to $W_{\lambda}(\mathrm{H}\,\alpha) = 365$ Å at the median redshift of z = 4.36. This value is in excellent agreement with previous estimates at similar redshifts. For example, Smit et al. (2016) find $W_{\lambda}(\mathrm{H}\,\alpha) = 325 \pm 22$ Å for a sample of N = 80 spectroscopically confirmed galaxies at $3.8 \le z \le 5.0$. In the same redshift range, Stark et al. (2013) report values of $W_{\lambda}(\mathrm{H}\,\alpha) \simeq 280 - 410$ Å (assuming $f_{\mathrm{H}\,\alpha} = 0.76$). Finally, we note that our constraints are also in good agreement with the redshift evolution for $W_{\lambda}(\mathrm{H}\,\alpha)$ derived by Mármol-Queraltó et al. (2016) across the redshift range $1 \le z \le 5$.

3.2.3 Null Sample Verification

As a sanity check of our method, we perform the same analysis on a sample of N=119 VANDELS star-forming galaxies selected in the redshift range $3.6 \le z_{\rm spec} \le 3.8$, within which the H α emission line does not contaminate the IRAC 3.6 μ m photometry and a photometric excess signature should not be detected². We apply the same procedures discussed above to this 'null' sample, deriving the blue histogram in Fig. 3. The null sample distribution is fully consistent with $\Delta[3.6\mu m]=0$, as expected. The median of the distribution is $\Delta[3.6\mu m]=0.05$ with $\sigma_{\rm MAD}=0.20$. For the reminder of this paper, we adopt $\sigma=0.20$ as the typical uncertainty on $\Delta[3.6\mu m]$.

3.3 Dust attenuation

To determine the intrinsic Ly α flux we first need an estimate of the intrinsic H α flux. The observed H α flux values are simply determined by multiplying $W_{\lambda}(H\alpha)$ by the continuum flux derived

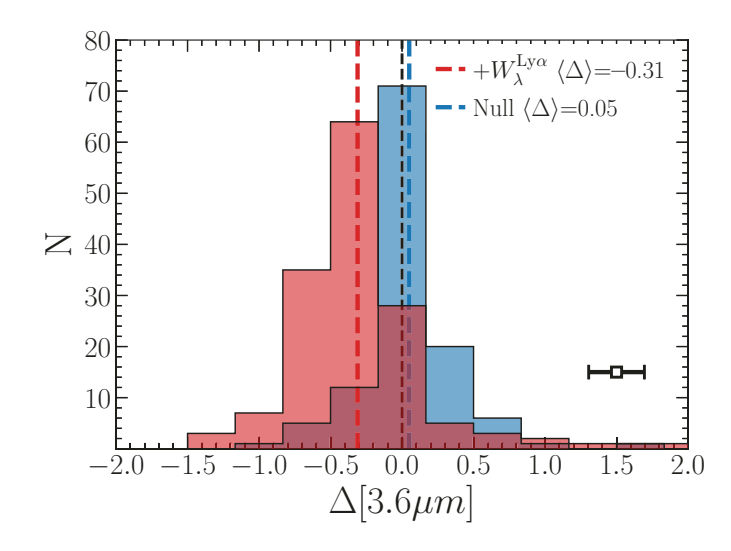


Figure 3. The distribution of $\Delta[3.6\mu\mathrm{m}]$, defined as the difference between the observed magnitude in the 3.6 $\mu\mathrm{m}$ filter and the predicted magnitude from the best-fitting SED model (see text for details). The red histogram shows the distribution of the N=152 galaxies with Ly α in emission. The median value of $\Delta[3.6\mu\mathrm{m}]=-0.31$, corresponds to $\langle W_{\lambda}(\mathrm{H}\,\alpha)\rangle\simeq365$ Å at the median redshift of the sample. The blue histogram shows the distribution for the null sample, for which the IRAC 3.6 $\mu\mathrm{m}$ filter is free from H α contamination. As expected, the null distribution is consistent with no flux excess. The $\Delta[3.6\mu\mathrm{m}]$ typical error is denoted by the black error bar.

from the best-fitting SED. To dust-correct the observed fluxes we use the prescription of Wuyts et al. (2013):

$$A_{\text{H}\alpha,\text{nebular}} = A_{\text{H}\alpha,\text{cont}} + 0.9A_{\text{H}\alpha,\text{cont}} - 0.15A_{\text{H}\alpha,\text{cont}}^2, \tag{3}$$

where $A_{\rm H~\alpha,cont}$ is the continuum attenuation at $\lambda_{\rm rest}=6563~{\rm \AA}$ determined from the FAST++ SED fitting to the VANDELS DR4 photometry (see Section 3.2.1). The additional attenuation is physically motivated by the increased dust obscuration surrounding young star-forming regions (e.g., Wuyts et al. 2013; Reddy et al. 2020). We note that this conversion explicitly assumes a Calzetti et al. (2000) attenuation law, which our previous work has shown to provide a good description of the average dust attenuation in VANDELS galaxies down to stellar masses of $\log({\rm M_{\star}/M_{\odot}}) \simeq 9.0$ (Cullen et al. 2018). We discuss the implications of assuming a steeper dust attenuation curve in Section 5.

As a further sanity check on our approach we compare the star-formation rates inferred from the dust-corrected H α emission and dust-corrected FUV stellar continuum in Fig. 4. Assuming that our SED-fitting and $W_{\lambda}(H\alpha)$ estimates are robust, there should be good agreement between these two star-formation-rate indicators that are both sensitive to star-formation on < 100 Myr timescales. To calculate the FUV-based star-formation rates we assume the Madau & Dickinson (2014) calibration

$$SFR_{UV}(M_{\odot}yr^{-1}) = 6.58 \times 10^{-29} L_{1500} (erg s^{-1}Hz^{-1}),$$
 (4)

where the dust-corrected L_{1500} is calculated from the best-fitting SED template determined in Section 3.2.1 using a 100 Å wide top-hat filter centered on $\lambda_{\rm rest} = 1500$ Å. To calculate the H α -based star-formation rate, we use the Reddy et al. (2018) calibration

$$SFR_{H\alpha}(M_{\odot}yr^{-1}) = 3.24 \times 10^{-42} L_{H\alpha}(erg s^{-1}),$$
 (5)

where $L_{\rm H~lpha}$ is the dust-corrected H lpha luminosity. It can be seen from Fig. 4 that the two estimates are qualitatively in excellent agreement. Fitting a fixed 1:1 relationship we find that the log(SFR_{H~\alpha}) estimates

² We note that this redshift range has been chosen such that none of the photometric filters are affected by nebular emission line contamination.

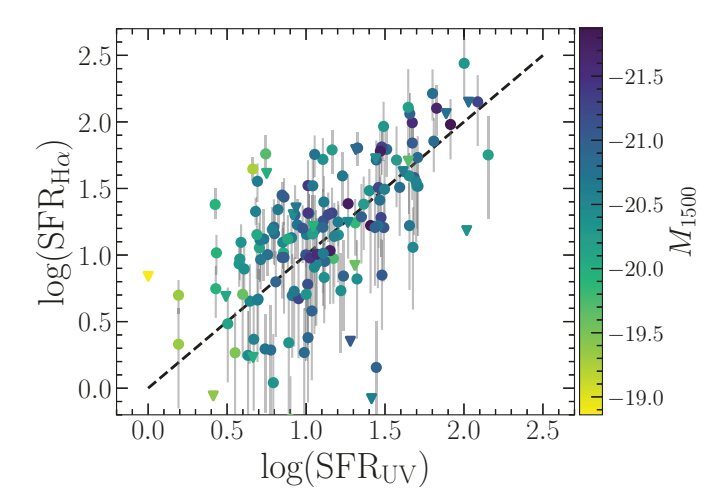


Figure 4. A comparison of the star-formation rates derived from our dust-corrected H α and UV (L_{1500}) luminosities. The one-to-one relation is shown as the dashed line. The broad agreement between the two estimates demonstrates the relative robustness of the $L_{{\rm H}\,\alpha}$ measurements.

are +0.05 dex (\simeq 10%) larger than the corresponding log(SFR_{UV}) estimates. However, we note that this systematic shift is much smaller than the statistical uncertainty on any individual measurement and globally decreasing the H α fluxes by \simeq 10 per cent does not affect any of the conclusions of this work.

3.4 Ly α escape fractions

The Ly α escape fraction is defined as the ratio between the observed and intrinsic Ly α flux. We determine intrinsic Ly α fluxes from the dust-corrected H α fluxes under the standard assumption of Case-B recombination (i.e., $F_{Ly \alpha,int} = 8.7 \times F_{H \alpha,int}$ Osterbrock 1989) which yields,

$$f_{\rm esc}^{\rm Ly\alpha} = \frac{F_{\rm Ly\,\alpha,obs}}{8.7 \times F_{\rm H\,\alpha,int}}.$$
 (6)

For the objects in our sample with $W_{\lambda}({\rm H}\,\alpha)$ < 0 (N=20) we calculate a 3σ upper limit on $f_{\rm esc}^{{\rm Ly}\,\alpha}$.

4 RESULTS

In this section we use our estimates of the observed Ly α and H α line fluxes to place constraints on the Ly α escape fraction and explore the relationship between $f_{\rm esc}^{{\rm Ly}\alpha}$ and $W_\lambda({\rm Ly}\,\alpha)$. At the end of the section we investigate whether the scatter around the $f_{\rm esc}^{{\rm Ly}\alpha}-W_\lambda({\rm Ly}\,\alpha)$ relation is in part driven by an underlying correlation between $f_{\rm esc}^{{\rm Ly}\alpha}$ and $f_{\rm esc}^{{\rm Ly}C}$.

4.1 A non-evolving $\mathbf{f}_{esc}^{Ly\alpha} - \mathbf{W}_{\lambda}(Ly\alpha)$ relation out to z=5

In the left-hand panel of Fig. 5 we plot $f_{\rm esc}^{{\rm Ly}\alpha}$ versus $W_{\lambda}({\rm Ly}\,\alpha)$ for our final sample of N=152 galaxies displaying Ly α in emission, along with our best-fitting relation (dashed line). Assuming the standard form of $f_{\rm esc}^{{\rm Ly}\alpha}=A\times W_{\lambda}({\rm Ly}\,\alpha)+B$, we determine the best-fitting relation to be:

$$f_{\rm esc}^{\rm Ly\alpha} = (3.8 \pm 0.3) \times 10^{-3} W_{\lambda}({\rm Ly}\,\alpha) - (1.0 \pm 0.7) \times 10^{-3},$$
 (7)

using the nested sampling algorithm density (Speagle 2020) with flat parameter priors. Here, the best-fitting slope and intercept are given by the median of the posterior distribution, with the 1σ errors designated as the $16^{\rm th}$ and $84^{\rm th}$ (68%) percentiles. We find evidence for a correlation at the $\simeq 10\sigma$ level, with $f_{\rm esc}^{\rm Ly}\alpha$ increasing monotonically from $\simeq 4\%$ to $\simeq 19\%$ over the range $10 \le W_{\lambda}({\rm Ly}\,\alpha) \le 50$ Å. As expected, our best-fitting relation is consistent with $f_{\rm esc}^{\rm Ly}\alpha = 0$ at $W_{\lambda}({\rm Ly}\,\alpha) = 0$.

In the right-hand panel of Fig. 5 we compare our new results to those of previous studies in the literature. Our results are in good agreement with the relation (red dashed line) derived by Sobral & Matthee (2019) for a combined sample of $z \simeq 2.2 - 2.6$ Ly α emitters and lower-redshift $z \sim 0 - 0.3$ 'high-redshift analogue' galaxies (including Green Pea galaxies, LyC leakers, and H α emitters; e.g., Hayes et al. 2013; Henry et al. 2015; Verhamme et al. 2017; Yang et al. 2017). Our results are also consistent with the stacking-based analysis of N = 99 Ly α emitters at a similar redshift to our sample ($z \simeq 4.9$) presented by Harikane et al. (2018). It can be seen from Fig. 5 that our best-fitting relation has a somewhat lower normalisation than both the Sobral & Matthee (2019) relation, and the binned Harikane et al. (2018) data. However, the relations are consistent at the $< 2\sigma$ level and, given the different selection and analysis techniques applied in these other studies (i.e., stacking), we do not consider the offset to be significant. Indeed, the normalisation and scatter of our individual measurements seem fully consistent with the z = 2.6 Ly α emitters presented in Pucha et al. (2022) and the z = 0 - 0.3 sample of Green Pea galaxies from Yang et al. (2017).

As discussed in Sobral & Matthee (2019) (see also Harikane et al. 2018) the observed $f_{\rm esc}^{{\rm Ly}\alpha} - W_{\lambda}({\rm Ly}\,\alpha)$ relation will be influenced by $\xi_{\rm ion}$ and dust attenuation, both of which are linked to metallicity. Given that these properties are known to evolve with redshift (Emami et al. 2020; Matthee et al. 2016), the apparent non-evolution of the $f_{\rm esc}^{{\rm Ly}\alpha} - W_{\lambda}({\rm Ly}\,\alpha)$ relation shown in Fig. 5 is worthy of further consideration

Crucially, the $z \sim 0 - 0.3$ galaxy samples we compare to in Fig. 5 have been deliberately selected to be analogues of high-redshift SFGs, such as those comprising our $z \approx 4 - 5$ sample from VAN-DELS. Using follow-up rest-frame optical spectroscopy of N = 33VANDELS SFGs at $z \ge 3$, Cullen et al. (2021) measured metallicites spanning $12 + \log(O/H) \simeq 7.6 - 8.2$, comparable to the range displayed by the Yang et al. (2017) Green Pea galaxy sample (also included in the $z \sim 0.3$ sub-sample of Sobral & Matthee 2019). We can further deduce that the low-redshift samples and our own $z \simeq 4-5$ sample will have comparable ξ_{ion} as a result of their similar metallicities (Cullen et al. 2020). Consequently, the lack of evolution in the $f_{\rm esc}^{{\rm Ly}\alpha}$ – $W_{\lambda}({\rm Ly}\,\alpha)$ relation shown in Fig. 5, simply indicates that the physical processes regulating the production and escape of Ly α photons in high-redshift SFGs are comparable to those in lowredshift analogues, deliberately selected to be a close match in terms of metallicity, ξ_{ion} and dust attenuation.

We note that, due to the depth of the VANDELS spectroscopy, we are able to trace the $f_{\rm esc}^{{\rm Ly}\alpha}-W_{\lambda}({\rm Ly}\,\alpha)$ relation for *individual* objects for the first time at these redshifts, as well as extending the relation to $W_{\lambda}({\rm Ly}\,\alpha)\lesssim 20$ Å, a regime previously only accessible to low-redshift studies. Our analysis demonstrates that at $z\geq 4$ the $f_{\rm esc}^{{\rm Ly}\alpha}-W_{\lambda}({\rm Ly}\,\alpha)$ relation extends down to $W_{\lambda}({\rm Ly}\,\alpha)\simeq 2-3$ Å, with our $f_{\rm esc}^{{\rm Ly}\alpha}$ constraints at these low $W_{\lambda}({\rm Ly}\,\alpha)$ values directly comparable to those derived in the low-redshift Universe (Fig. 5).

Overall, our analysis indicates that the $f_{\rm esc}^{{\rm Ly}\,\alpha}-W_{\lambda}({\rm Ly}\,\alpha)$ relation for SFGs at $z\simeq 4-5$ is indistinguishable from that followed by

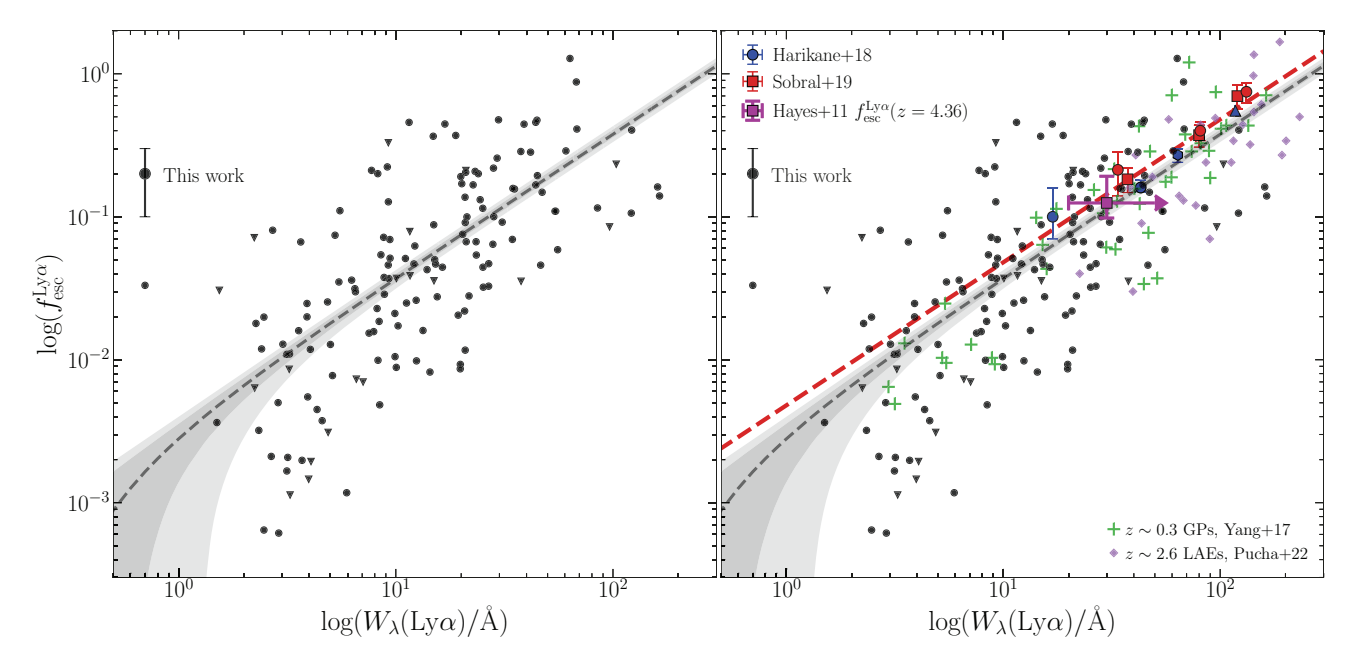


Figure 5. The left-hand panel shows the relationship between $f_{\rm esc}^{\rm Ly\alpha}$ and $W_{\lambda}({\rm Ly}\,\alpha)$ for the final sample of N=152 VANDELS galaxies at 3.85 $\leq z_{\rm spec} \leq 4.85$ with $W_{\lambda}({\rm Ly}\,\alpha) > 0$ Å. The best-fitting relation is shown as the dashed line and $f_{\rm esc}^{\rm Ly\alpha}$ upper limits are shown as triangles (see text for details). The right-hand panel shows a comparison between our new results and those of previous literature studies. The best-fitting relation from Sobral & Matthee (2019), based on the combined sample of lower-redshift $z \sim 0-0.3$ 'high-redshift analogue' galaxies and $z \sim 2.2-2.6$ Lyman-alpha emitters (LAEs) (see Sobral et al. 2017 using stacks; and Trainor et al. 2015 using binning; red squares and circles, respectively), is shown as a red dashed line. A compilation of literature results based on LAE samples, including those from Harikane et al. (2018) (LAE stacks, blue circles) at comparable redshifts ($z \sim 4.9$), and constraints on individual $z \sim 2.6$ LAEs (purple diamonds) from Pucha et al. (2022), are also plotted. A sample of low-redshift ($z \sim 0.3$) Green Pea galaxies (Yang et al. 2017) are shown as green crosses. The magenta square indicates the predicted $f_{\rm esc}^{\rm Ly\alpha}$ value at the median redshift of the sample, $\langle z_{\rm spec} \rangle \simeq 4.36$, according to the $f_{\rm esc}^{\rm Ly\alpha} - z$ relation of Hayes et al. (2011).

their low-redshift analogues. This implies that the physical processes determining the production and escape of Ly α photons from low metallicity, high $\xi_{\rm ion}$ galaxies do not vary significantly over $\simeq 11$ Gyr (i.e., $\simeq 90$ per cent) of cosmic time.

4.1.1 Average $f_{\rm esc}^{{\rm Ly}\,\alpha}$ of ${\rm Ly}\,\alpha$ emitters

It is interesting to compare our results for individual objects to previous constraints on the population averaged Ly α escape fraction. Based on a compilation of Ly α , UV, and H α luminosity functions, Hayes et al. (2011) determined that the redshift evolution of $\langle f_{\rm esc}^{\rm Ly\alpha}\rangle$ is well-described by a power law of the form $\propto (1+z)^{2.57}$, with $\langle f_{\rm esc}^{\rm Ly\alpha}\rangle$ evolving from $\langle f_{\rm esc}^{\rm Ly\alpha}\rangle \simeq 0.01$ at $z\simeq 0.3$ up to $\langle f_{\rm esc}^{\rm Ly\alpha}\rangle \simeq 0.4$ at $z\simeq 6$. At the median redshift of our final sample $(\langle z_{\rm spec}\rangle = 4.36)$, the Hayes et al. (2011) relation predicts $\langle f_{\rm esc}^{\rm Ly\alpha}\rangle \simeq 0.13$ which is indicated by the purple data point in the right-hand panel of Fig. 5.

This average value is clearly in good agreement with the high $W_{\lambda}(\mathrm{Ly}\,\alpha)$ objects in our sample, consistent with the fact that the galaxies used to derive the Hayes et al. (2011) relation were typically $\mathrm{Ly}\,\alpha$ emitters with $W_{\lambda}(\mathrm{Ly}\,\alpha) > 20$ Å. Restricting our sample to objects with $W_{\lambda}(\mathrm{Ly}\,\alpha) > 20$ Å we find a median value of $\langle f_{\mathrm{esc}}^{\mathrm{Ly}\,\alpha} \rangle \simeq 0.12$, in excellent agreement with the Hayes et al. (2011) prediction. This consistency is encouraging, given that the two estimates originate from completely independent methods.

4.2 Connecting Ly α and LyC escape

Although the results presented in Fig. 5 show a strong correlation between $f_{\rm esc}^{{\rm Ly}\alpha}$ and $W_{\lambda}({\rm Ly}\,\alpha)$, there is clearly a large amount of asso-

ciated scatter ($\simeq 0.5$ dex). Some fraction of this scatter is attributable to measurement uncertainties, given that our individual estimates of $f_{\rm esc}^{\rm Ly\alpha}$ are undoubtedly noisy. However, at a given value of $W_{\lambda}({\rm Ly}\,\alpha)$ we also expect *intrinsic* scatter in $f_{\rm esc}^{\rm Ly\alpha}$ due to variations in the stellar populations and dust/gas properties. One way of exploring the range of $f_{\rm esc}^{\rm Ly\alpha}$ at a given value of $W_{\lambda}({\rm Ly}\,\alpha)$ is to investigate the link between $f_{\rm esc}^{\rm Ly\alpha}$ and $f_{\rm esc}^{\rm LyC}$.

A growing body of literature has empirically established a strong positive correlation between $W_{\lambda}(\text{Ly}\,\alpha)$ (i.e., $f_{\text{esc}}^{\text{Ly}\alpha}$) and $f_{\text{esc}}^{\text{Ly}\text{C}}$ in high-redshift star-forming galaxies, either via direct measurements of LyC emission (e.g., Marchi et al. 2018; Steidel et al. 2018; Pahl et al. 2021; Begley et al. 2022), or via indirect studies characterising the H I covering fraction (Shapley et al. 2003; Gazagnes et al. 2020; Saldana-Lopez et al. 2022a). A similarly strong connection is also observed at low redshifts (e.g., Vanzella et al. 2016; Verhamme et al. 2017; Flury et al. 2022b). This link can be explained by the similar escape path of LyC and Ly α photons through low dust/H I columndensity channels (e.g., Dijkstra et al. 2016; Jaskot et al. 2019), a picture supported by detailed radiative transfer simulations (e.g., Cen & Kimm 2015; Kimm et al. 2019).

Below, we use composites of our VANDELS spectra to explore this connection further. Rather than using $W_{\lambda}(\mathrm{Ly}\,\alpha)$ as a proxy for $f_{\mathrm{esc}}^{\mathrm{Ly}\,\alpha}$, we can take advantage of our *individual* $f_{\mathrm{esc}}^{\mathrm{Ly}\,\alpha}$ escape estimates to trace the connection between $f_{\mathrm{esc}}^{\mathrm{Ly}\,\alpha}$ and the properties of the ISM measured from deep rest-frame FUV spectra. This in turn allows us to connect the escape of Ly α and LyC photons using the correlation established between the equivalent width of low-ionization-state FUV ISM absorption lines and $f_{\mathrm{esc}}^{\mathrm{LyC}}$ by Saldana-Lopez et al. (2022a).

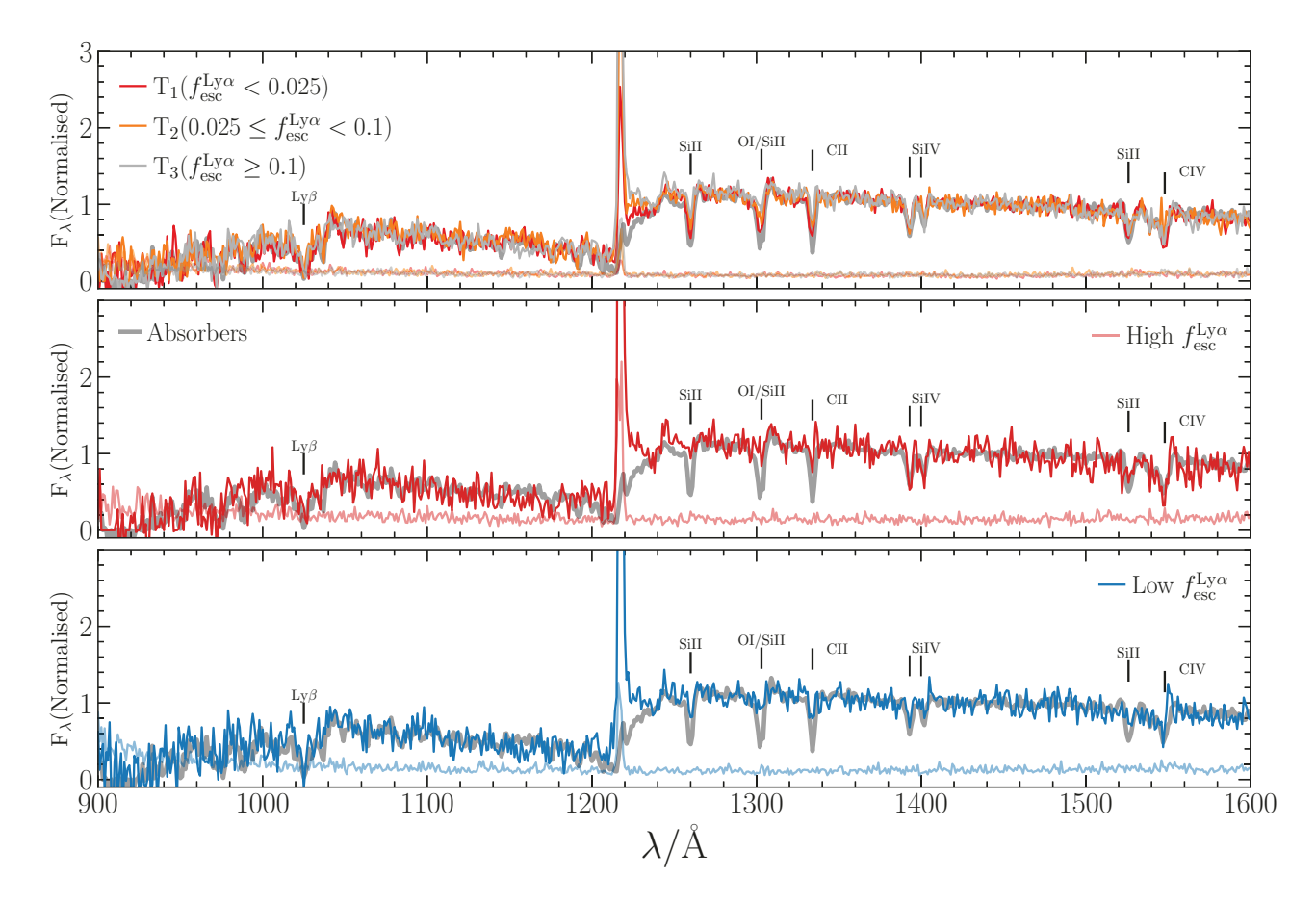


Figure 6. The top panel shows an overlay of four composite VANDELS spectra. The dark grey composite is a stack of N=111 VANDELS galaxies within the redshift range $3.85 \le z_{\rm spec} \le 4.95$ that display Ly α in absorption (i.e. $W_{\rm Ly\,\alpha} < 0$). This composite is shown in all three panels. The red, orange and light grey composites are constructed from three equally-occupied bins of $f_{\rm esc}^{\rm Ly\alpha}$ ($T_1:f_{\rm esc}^{\rm Ly\alpha} < 0.025$, $T_2:0.025 \le f_{\rm esc}^{\rm Ly\alpha} < 0.1$ and $T_3:f_{\rm esc}^{\rm Ly\alpha} \ge 0.1$). The middle and bottom panels show composites formed from objects with $W_{\rm Ly\,\alpha} \ge 25$ Å, that have been split into high- and low- $f_{\rm esc}^{\rm Ly\alpha}$ sub-samples at a threshold of $f_{\rm esc}^{\rm Ly\alpha} \ge 0.2$. This selection ensures that both composites have approximately the same equivalent width $(\Delta(W_{\lambda}({\rm Ly\,\alpha})) < 5$ Å) but widely different values of $f_{\rm esc}^{\rm Ly\alpha}$ (see text for details). Notable absorption features are highlighted with black vertical lines (e.g. ${\rm Siii}\lambda 1260$, ${\rm Cii}\lambda 1334$, ${\rm Oi}/{\rm Siii}\lambda 1303$, and ${\rm Siii}\lambda 1526$).

4.2.1 Constructing VANDELS composite spectra

To maximise the available signal-to-noise of our VANDELS spectra we create stacked FUV composites following a similar procedure to that outlined in Cullen et al. (2019). To create the composite spectra of a given ensemble of galaxies, we first shift each individual spectrum to the rest-frame using its spectroscopic redshift and normalise to the median flux in the range $1420 \leq \lambda_{rest} \leq 1480$ Å. The individual flux elements of each spectra are then binned onto the desired wavelength grid of the final stack (1 Å/pix). The flux of each pixel in the composite spectrum is given by the median of the individual fluxes after 3σ outliers have been sigma clipped. The associated error spectrum is estimated by bootstrap re-sampling of the fluxes in each wavelength bin, taking the standard deviation of each as the 1σ uncertainty.

4.2.2 The strength of ISM absorption features

The top panel of Fig. 6 is an overlay of four composite spectra. The dark-grey spectrum is a composite of the N=111 VANDELS galaxies within the redshift range $3.85 \le z_{\rm spec} \le 4.95$ that display Ly α in absorption. The other three spectra are composites obtained by splitting our final sample of N=152 VANDELS galax-

ies with Ly α in emission into three equally occupied bins of $f_{\rm esc}^{{\rm Ly}\,\alpha}$ (T₁ = $f_{\rm esc}^{{\rm Ly}\,\alpha}$ < 0.025, T₂ = 0.025 $\leq f_{\rm esc}^{{\rm Ly}\,\alpha}$ < 0.1 and T₃ = $f_{\rm esc}^{{\rm Ly}\,\alpha}$ \geq 0.1). Some key features are immediately visible by eye. Compared to

Some key features are immediately visible by eye. Compared to the composite spectrum of galaxies displaying Ly α in absorption, it is clear that the Ly α emission composites display progressively weaker low-ionization-state ISM absorption lines as a function of increasing $f_{\rm esc}^{\rm Ly}\alpha$. The weak LIS ISM lines are a clear signature of a low covering fraction³ of neutral H I gas, one of the key requirements for an increased escape of Ly α /LyC photons (Reddy et al. 2016; Saldana-Lopez et al. 2022b).

Although the LIS ISM features in the composite spectra shown in Fig. 6 behave as expected, the correlation between $f_{\rm esc}^{\rm Ly\,\alpha}$ and $W_{\lambda}({\rm Ly\,\alpha})$ shown in Fig. 5 means that it is not clear which of the two parameters is driving the observed trend. To investigate this issue, we also create two composite spectra at *fixed* $W_{\lambda}({\rm Ly\,\alpha})$. By selecting

³ We highlight that the LIS lines are saturated and therefore act as tracers of the covering fraction, C_f (see also Section 4.2.4). For the Si Π line species, we measure $W_{1260}({\rm Si}\,\Pi)/W_{1526}({\rm Si}\,\Pi)\lesssim 1.6\pm0.5$ for all three $f_{\rm esc}^{\rm Ly}$ α-binned composites (top panel, Fig. 6). In the optically-thin regime $W_{1260}({\rm Si}\,\Pi)/W_{1526}({\rm Si}\,\Pi)=6.0$ (Shapley et al. 2003; Erb et al. 2010), which is inconsistent with the data.

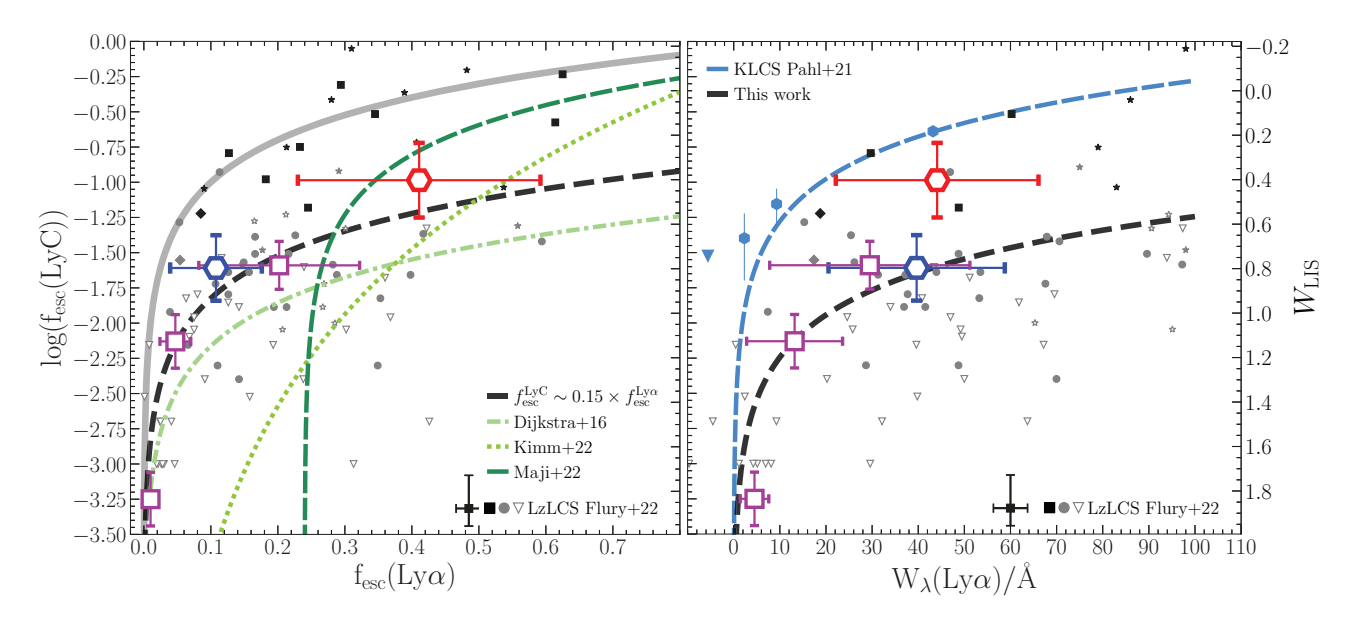


Figure 7. The left-hand panel shows the relationship between $f_{\rm esc}^{\rm LyC}$ and $f_{\rm esc}^{\rm LyC}$ based on the composite spectra shown in Fig. 6, where $f_{\rm esc}^{\rm LyC}$ has been estimated based on $W_{\rm LIS}$ measurements (shown on the secondary y-axis on the right-hand side) using the $W_{\rm LIS}-f_{\rm esc}^{\rm LyC}$ relation from Saldana-Lopez et al. (2022a). The three composites based on equally-occupied bins of $f_{\rm esc}^{\rm LyC}$ are shown as purple squares, while the high- and low- $f_{\rm esc}^{\rm LyC}$ composites at a constant value of $W_{\Lambda}({\rm Ly}\,\alpha)$ are shown as red and blue hexagons. The $f_{\rm esc}^{\rm LyC}$ data from the LzLCS sample for strong Lyman continuum emitters (LCEs), weak LCEs and non-emitters are shown as small filled black, filled grey and open grey markers, respectively (typical uncertainties are shown in the lower right, see Flury et al. 2022a,b, for further details). Simulation-derived $f_{\rm esc}^{\rm LyC}-f_{\rm esc}^{\rm LyC}$ relations are shown as green lines (Dijkstra et al. 2016, dash-dotted; Kimm et al. 2022, dotted; Maji et al. 2022, dashed). The 1:1 relation is shown as thick grey line and $f_{\rm esc}^{\rm LyC} \simeq 0.15 \times f_{\rm esc}^{\rm LyC}$ is shown as a dashed black line. The right-hand panel shows the same composite-based $f_{\rm esc}^{\rm LyC}$ constraints as a function of $W_{\Lambda}(\rm Ly\,\alpha)$, including values for the LzLCS sample. The $W_{\Lambda}(\rm Ly\,\alpha)-f_{\rm esc}^{\rm LyC}$ relation derived at $z\simeq 3$ from the KLCS (Pahl et al. 2021) is shown as the dashed blue line, with the blue markers indicating constraints for composite KLCS spectra as a function of $W_{\Lambda}(\rm Ly\,\alpha)$. The dashed black line shows the relationship $f_{\rm esc}^{\rm LyC}\simeq 0.0005 f_{\rm esc}^{\rm LyC}$, derived by combining our best-fitting $f_{\rm esc}^{\rm LyC}-W_{\Lambda}(\rm Ly\,\alpha)$ relationship (see Fig. 5) with $f_{\rm esc}^{\rm LyC}\simeq 0.15 f_{\rm esc}^{\rm LyC}$.

all galaxies with $W_{\lambda}(\mathrm{Ly}\,\alpha) \geq 25$ Å and splitting into high- $f_{\mathrm{esc}}^{\mathrm{Ly}\alpha}$ and low- $f_{\mathrm{esc}}^{\mathrm{Ly}\alpha}$ sub-sets at a threshold of $f_{\mathrm{esc}}^{\mathrm{Ly}\alpha} \geq 0.2$, it was possible to produce two composites with similar $W_{\lambda}(\mathrm{Ly}\,\alpha)$ and sufficiently high signal-to-noise to allow measurements of the LIS absorption features. The high- $f_{\mathrm{esc}}^{\mathrm{Ly}\alpha}$ and low- $f_{\mathrm{esc}}^{\mathrm{Ly}\alpha}$ composites are shown in the middle and bottom panel of Fig. 6, respectively. The high- $f_{\mathrm{esc}}^{\mathrm{Ly}\alpha}$ composite contains N=13 galaxies with median (and σ_{MAD}) values of $\langle f_{\mathrm{esc}}^{\mathrm{Ly}\alpha} \rangle = 0.41 \pm 0.18$ and $\langle W_{\lambda}(\mathrm{Ly}\,\alpha) \rangle = 44.1 \pm 21.9$ Å. The low- $f_{\mathrm{esc}}^{\mathrm{Ly}\alpha}$ composite contains N=22 galaxies with $\langle f_{\mathrm{esc}}^{\mathrm{Ly}\alpha} \rangle = 0.11 \pm 0.07$ and $\langle W_{\lambda}(\mathrm{Ly}\,\alpha) \rangle = 39.7 \pm 19.1$ Å.

4.2.3 LIS equivalent widths

For each spectrum, we measure equivalent widths for the Si II λ 1260, C II λ 1334, and the O I λ 1303+Si II λ 1303 low-ionization state ISM absorption features (with the final feature blended due to the VANDELS $R \simeq 600$ spectral resolution; see Fig. 6). The equivalent widths are calculated numerically according to the following equation:

$$W_{\rm LIS} = \int_{\Delta \lambda} \left(1 - \frac{f_{\rm obs}}{f_{\rm cont}} \right) d\lambda, \tag{8}$$

where $f_{\rm obs}$ is the flux density of observed spectrum, $f_{\rm cont}$ is the underlying stellar continuum flux density, and $\Delta\lambda$ is the width of the region over which the numerical integration is performed, which we set to a default value of $\pm 500\,{\rm km\,s^{-1}}$. The values of $\Delta\lambda$ and λ_0 are manually adjusted for each line measurement to account for velocity offsets or nearby noise spikes. The stellar continuum component is calculated by fitting a $f_{\lambda} \propto \lambda^{\beta}$ power law to the continuum either side

of the line, typically spanning $\pm 4500\,\mathrm{km\,s^{-1}}$ ($\gtrsim 20\,\mathrm{Å}$). Uncertainties were calculated using a Monte Carlo procedure.

4.2.4 The connection between $f_{\rm esc}^{{\rm Ly}\,\alpha}$ and the ISM ionization state

Qualitatively, it can be seen from Fig. 6 that the low-ionization ISM lines are somewhat weaker in the high- $f_{\rm esc}^{{\rm Ly}\alpha}$ composite than in the low- $f_{\rm esc}^{{\rm Ly}\alpha}$ composite. In addition, the high-ionization Si IV $\lambda\lambda$ 1393, 1402 and blended C IV $\lambda\lambda$ 1548, 1550 absorption lines appear to be more prominent in the high- $f_{\rm esc}^{{\rm Ly}\alpha}$ composite. That is, at fixed $W_{\lambda}({\rm Ly}\,\alpha)$, galaxies with higher $f_{\rm esc}^{{\rm Ly}\alpha}$ appear to show signatures consistent with having a lower covering fraction of neutral gas and a higher covering fraction of ionized gas.

Using the procedure outlined above, we measure equivalent widths for the Si IV $\lambda\lambda$ 1393, 1402 doublet in the high- $f_{\rm esc}^{Ly\alpha}$ composite of $W_{1393}({\rm Si\ IV})=1.36\pm0.33$ Å and $W_{1402}({\rm Si\ IV})=1.23\pm0.34$ Å. Similarly, in the low- $f_{\rm esc}^{Ly\alpha}$ composite we measure $W_{1393}({\rm Si\ IV})=0.74\pm0.31$ Å and $W_{1402}({\rm Si\ IV})=0.51\pm0.20$ Å.

The line ratio in the Si IV $\lambda\lambda$ 1393, 1402 doublet can be used to infer whether it originates from optically thin or optically-thick ISM gas. In the optically-thin regime, the doublet ratio will be $W_{1393}(\text{Si IV})/W_{1402}(\text{Si IV}) \approx 2$ (Shapley et al. 2003; Berry et al. 2012), whereas ratios of $W_{1393}(\text{Si IV})/W_{1402}(\text{Si IV}) \approx 1$ are indicative of saturated lines arising from an optically thick, high-ionization-state ISM. For the high- and low- $f_{\text{esc}}^{\text{Ly}\alpha}$ composites we find doublet ratios of $W_{1393}(\text{Si IV})/W_{1402}(\text{Si IV}) = 1.1 \pm 0.4$ and $W_{1393}(\text{Si IV})/W_{1402}(\text{Si IV}) = 1.45 \pm 0.8$, respectively. For the low- $f_{\text{esc}}^{\text{Ly}\alpha}$ composite we are clearly unable to conclude anything regarding

optical depth, as the doublet ratio is fully consistent with both the optically thin and optically-thick regimes. On the other hand, despite the obvious uncertainty, the high- $f_{\rm esc}^{{\rm Ly}\alpha}$ doublet ratio is more consistent with saturation, providing evidence of a more-highly ionized ISM environment in the galaxy composite with higher $f_{\rm esc}^{{\rm Ly}\alpha}$.

This conclusion is further strengthened by comparing the UV spectral slopes of the high- and low- $f_{\rm esc}^{{\rm Ly}\alpha}$ composites. Fitting a power-law of the form $f_{\lambda} \propto \lambda^{\beta}$, we find the high- $f_{\rm esc}^{{\rm Ly}\alpha}$ composite ($\beta=-1.8\pm0.2$) to be bluer than its low- $f_{\rm esc}^{{\rm Ly}\alpha}$ counterpart ($\beta=-1.4\pm0.1$). This spectral slope difference is consistent with recent results (see Gazagnes et al. 2020; Begley et al. 2022) indicating that galaxies with bluer UV slopes are more likely to display more-highly ionizing environments (and higher $f_{\rm esc}^{{\rm LyC}}$).

4.2.5 The connection between $f_{\rm esc}^{\rm Ly\alpha}$ and $f_{\rm esc}^{\rm LyC}$

Recently, Saldana-Lopez et al. (2022a) have identified a strong relationship between $f_{\rm esc}^{\rm LyC}$ and the equivalent width of low-ionization absorption lines ($W_{\rm LIS}$), calibrated using the LzLCS dataset (see also Chisholm et al. 2018; Gazagnes et al. 2020). Using this relationship, we are able to estimate the value of $f_{\rm esc}^{\rm LyC}$ for the composite spectra shown in Fig. 6.

We calculate the inverse-variance weighted mean across the Si $\pi\lambda 1260$, C $\pi\lambda 1334$, O $t\lambda 1303+$ Si $\pi\lambda 1303$ and the Si $t\lambda 1526$ features⁴. For the three composite spectra shown in the upper panel of Fig. 6, we measure values of $W_{LIS} = 1.84 \pm 0.12$ Å, 1.13 ± 0.12 Å and 0.78 ± 0.17 Å, in order of increasing $f_{\rm esc}^{\rm Ly\alpha}$. Likewise, for the high- $f_{\rm esc}^{\rm Ly\alpha}$ and low- $f_{\rm esc}^{\rm Ly\alpha}$ composites shown in the middle and bottom panels of Fig. 6, we measure $W_{\rm LIS} = 0.40 \pm 0.17$ Å and 0.80 ± 0.15 Å, respectively. We show the corresponding values of $f_{\rm esc}^{\rm LyC}$ in the left-hand panel of Fig. 7, having employed Eqn. 11 from Saldana-Lopez et al. (2022a) to map between $W_{\rm LIS}$ and $f_{\rm esc}^{\rm LyC}$. For galaxies at $z \approx 4-5$, our results indicate that $f_{\rm esc}^{\rm Ly\alpha}$ and $f_{\rm esc}^{\rm LyC}$ are positively correlated and follow a relationship of the form $f_{\rm esc}^{\rm LyC} \approx 0.15 f_{\rm esc}^{\rm Ly\alpha}$. Crucially, we can be confident that the $f_{\rm esc}^{\rm LyC} - f_{\rm esc}^{\rm Ly\alpha}$ relation is not being driven by $W_{\lambda}({\rm Ly}\,\alpha)$, given that the $f_{\rm esc}^{\rm LyC}$ and $f_{\rm esc}^{\rm Ly\alpha}$ values derived for the two equal- $W_{\lambda}({\rm Ly}\,\alpha)$ composites follow the same relation (red and blue hexagons in Fig. 7). We discuss the physical interpretation and implications of this result in Section 5.

4.2.6 Comparing $f_{\rm esc}^{\rm LyC}$ inferred from $W_{\rm LIS}$ to direct $f_{\rm esc}^{\rm LyC}$ observations at z>3

Finally, in the right-hand panel of Fig. 7 we compare the $f_{\rm esc}^{\rm LyC}-W_{\lambda}({\rm Ly}\,\alpha)$ relationship of our $z\simeq 4-5$ sample, as estimated from LIS absorption-line strength, to more direct measurements at low and high redshift. Our results are consistent with a relation of the form $f_{\rm esc}^{\rm LyC}\simeq 0.0005W_{\lambda}({\rm Ly}\,\alpha)$ (black dashed line), which is simply the result of combining the $f_{\rm esc}^{\rm Ly\alpha}-W_{\lambda}({\rm Ly}\,\alpha)$ relation shown in

Fig. 5 with the $f_{\rm esc}^{\rm LyC}-f_{\rm esc}^{\rm Ly\alpha}$ relation shown in the left-hand panel of Fig. 7. As expected, given the origin of the $W_{\rm LIS}-f_{\rm esc}^{\rm LyC}$ calibration from Saldana-Lopez et al. (2022a), our results are consistent with the $f_{\rm esc}^{\rm LyC}-W_{\lambda}({\rm Ly}\,\alpha)$ measurements from the low-redshift LzLCS survey at z=0.2-0.4 (Flury et al. 2022a), both in terms of normalisation and scatter

In contrast, our new results are systematically lower than the $f_{\rm esc}^{\rm LyC}-W_{\lambda}({\rm Ly}\,\alpha)$ relation derived by Pahl et al. (2021). The $W_{\lambda}({\rm Ly}\,\alpha)-f_{\rm esc}^{\rm LyC}$ constraints from Pahl et al. (2021) are based on direct measurements of $W_{\lambda}({\rm Ly}\,\alpha)$ and LyC flux from extremely deep spectra of galaxies at $z\simeq 3$ (KLCS survey; Steidel et al. 2018) and correspond to $f_{\rm esc}^{\rm LyC}\simeq 0.0053W_{\lambda}({\rm Ly}\,\alpha)$ (blue dashed line). Although our new results at $z\simeq 4-5$ follow a $f_{\rm esc}^{\rm LyC}-W_{\lambda}({\rm Ly}\,\alpha)$ relation with the same functional form, the use of the low-redshift $W_{\rm LIS}-f_{\rm esc}^{\rm LyC}$ calibration from Saldana-Lopez et al. (2022a) leads to a normalisation that is a factor of $\simeq 10$ lower.

To confirm the presence of this normalisation discrepancy, we construct an additional composite VANDELS spectrum from the upper $W_{\lambda}(\mathrm{Ly}\,\alpha)$ sub-sample defined in Begley et al. (2022) (with SFGs in the redshift range 3.35 < z_{spec} < 3.95 and $W_{\lambda}(\mathrm{Ly}\,\alpha)$ spanning $-6\,\mathrm{\mathring{A}} \lesssim W_{\lambda}(\mathrm{Ly}\,\alpha) \lesssim 93\,\mathrm{\mathring{A}}$), and measure $f_{\mathrm{esc}}^{\mathrm{LyC}} \simeq 0.005$ (corresponding to $W_{\mathrm{LIS}} \simeq 1.2\,\mathrm{\mathring{A}}$), following the same method detailed in Section 4.2.5. Comparing with the direct photometry-based constraint of $f_{\mathrm{esc}}^{\mathrm{LyC}} = 0.12^{+0.06}_{-0.04}$ measured in Begley et al. (2022), we again find independent evidence for a significant (factor $\gtrsim 10-20$) normalisation offset at $z \geq 3$ between indirect $f_{\mathrm{esc}}^{\mathrm{LyC}}$ estimates (using the low-redshift $f_{\mathrm{esc}}^{\mathrm{LyC}} - W_{\mathrm{LIS}}$ calibration) and direct estimates of $f_{\mathrm{esc}}^{\mathrm{LyC}}$ from deep U-band imaging/spectroscopy.

To achieve consistency, it seems likely that the normalisation of the $W_{\rm LIS}-f_{\rm esc}^{\rm LyC}$ relation must evolve with redshift to permit significantly higher values of $f_{\rm esc}^{\rm Ly\alpha}$ for a given value of $W_{\rm LIS}$. The offset in normalisation was previously noted and discussed in detail by Saldana-Lopez et al. (2022a). In Section 5 we provide a brief review of the systematics that are likely to be responsible.

5 DISCUSSION

The results presented in Fig. 5 demonstrate that our sample of $z \simeq 4-5$ galaxies displays a $f_{\rm esc}^{{\rm Ly}\alpha}-W_{\lambda}({\rm Ly}\,\alpha)$ relation that is very similar to the relation observed at lower redshifts. We also show in Fig. 6 that some of the scatter around this relationship is connected to a genuine range in $f_{\rm esc}^{{\rm Ly}\alpha}$ at a given value of $W_{\lambda}({\rm Ly}\,\alpha)$. This figure demonstrates that empirically, composite spectra binned as a function of $f_{\rm esc}^{{\rm Ly}\alpha}$ display the expected anti-correlation between $f_{\rm esc}^{{\rm Ly}\alpha}$ and the depth of the LIS absorption features that are believed to be tracers of $f_{\rm esc}^{{\rm Ly}C}$ (and $f_{\rm esc}^{{\rm Ly}\alpha}$). Based on a low-redshift calibration between $W_{\rm LIS}$ and $f_{\rm esc}^{{\rm Ly}C}$ from Saldana-Lopez et al. (2022a), the results presented in the left-hand panel of Fig. 7 show that $f_{\rm esc}^{{\rm Ly}C}$ and $f_{\rm esc}^{{\rm Ly}\alpha}$ are strongly correlated, following a relation consistent with $f_{\rm esc}^{{\rm Ly}C} \simeq 0.15 f_{\rm esc}^{{\rm Ly}\alpha}$. Importantly, the results derived from the composite spectra designed to have the same $W_{\lambda}({\rm Ly}\,\alpha)$ indicate that this correlation is not being driven by a secondary correlation between $f_{\rm esc}^{{\rm Ly}\alpha}$ and $W_{\lambda}({\rm Ly}\,\alpha)$.

These results are qualitatively consistent with the predictions of so-called 'picket-fence' models, in which the geometry and physical conditions of the ISM gas in the immediate vicinity of star-forming regions play a decisive role in governing the escape of ionizing and Ly α photons (Shapley et al. 2003; Chisholm et al. 2018; Gazagnes et al. 2020). These models suggest $f_{\rm esc}^{\rm LyC}$ is primarily dictated by the

⁴ These lines represent a subset of the full suite of LIS features originally employed in Saldana-Lopez et al. (2022a). Specifically, we do not include measurements of the Si $\Pi \lambda 989$, Si $\Pi \lambda 1020$, and Si $\Pi \lambda \lambda 1190$, 1193 features and in turn avoid potential systematic biases that may arise from the need to correct for the impact of IGM+CGM absorption blueward of Ly α. We also exclude the Si $\Pi \lambda 1526$ absorption feature from the high- $f_{\rm esc}^{\rm Ly}$ composite spectra due to a suspected noise spike in the immediate wavelength vicinity affecting the measurement.

covering fraction of optically thick H I gas $(C_f^{\rm H\,I})$, with LyC and Ly α photons escaping through channels of low-column-density and/or high-ionization-state gas. These channels become more abundant with decreasing $C_f^{\rm H\,I}$, leading to a $f_{\rm esc}^{\rm LyC} \propto (1-C_f^{\rm H\,I})$ relationship (Verhamme et al. 2017; Steidel et al. 2018; Saldana-Lopez et al. 2022a).

Our results are, to first order, also consistent with the overall trends expected from simulations. In the left-hand panel of Fig. 7 we show the predictions of three independent simulations. The dashed green line shows the $f_{\rm esc}^{\rm Ly} - f_{\rm esc}^{\rm Ly}$ relation from Maji et al. (2022), based on the SPHINX suite of cosmological radiation-hydrodynamical simulations (Rosdahl et al. 2018). The dash-dotted green line shows the relation from Dijkstra et al. (2016), derived from a suite of clumpy ISM models covering a wide range of physical conditions. Finally, the dotted green line shows the relation from the Kimm et al. (2022) high-resolution simulations of giant molecular clouds, including stellar feedback, that suggest a steeper relationship of the form $f_{\rm esc}^{\rm LyC} \simeq (f_{\rm esc}^{\rm Ly\alpha})^{3.7}$. All three studies show trends qualitatively consistent with our results, albeit with offsets in absolute $f_{\rm esc}^{\rm LyC}$ values. The Maji et al. (2022) relation appears to imply that a threshold of $f_{\rm esc}^{{\rm Ly}\alpha} \simeq 0.2$ must be met before LyC leakage can occur, inconsistent with our low- $f_{\rm esc}^{{\rm Ly}\alpha}$ constraints. However, Maji et al. (2022) also show that a number of their simulated galaxies do occupy this region of $f_{\rm esc}^{\rm Ly} - f_{\rm esc}^{\rm Ly}$ parameter space and that there is generally a large amount of scatter in the relation, consistent with the low-redshift

A final issue that merits discussion is the offset in absolute $f_{\rm esc}^{\rm LyC}$ inferred indirectly from low-ionization FUV absorption lines and direct estimates of $f_{\rm esc}^{\rm LyC}$ at z>3 (Steidel et al. 2018; Pahl et al. 2021; Begley et al. 2022). This issue has been explored in detail by Saldana-Lopez et al. (2022a) and we refer the reader to that paper for a thorough discussion. However, there are three obvious systematic effects that are worth briefly discussing here.

Firstly, in general, it is worth remembering that the $W_{\rm LIS}-f_{\rm esc}^{\rm LyC}$ relation used here was calibrated using a sample of rare, low-redshift LCE candidates from the LzLCS (Saldana-Lopez et al. 2022a). These galaxies will not be perfect analogues for the z>3 star-forming population in terms of evolutionary stage, star-formation rate, metallicity or dust enrichment. As such, it is not unreasonable to think that the appropriate absolute calibration of the $W_{\rm LIS}-f_{\rm esc}^{\rm LyC}$ at z>3 may well be significantly different from that which is appropriate at low redshifts.

A second potentially important systematic is the choice of model used to describe the ISM gas geometry. In the 'holes' geometry adopted by Pahl et al. (2021), the dust and H I gas reside in pockets around star-forming regions and are optically thick to ionizing radiation. In this geometry, the LyC escape fraction is simply given as $f_{\rm esc}^{\rm LyC} = (1-C_f^{\rm H\,I})$, where $C_f^{\rm H\,I}$ is the covering fraction of neutral hydrogen gas. Recently, Chisholm et al. (2018) have suggested that this model, by not considering the effects of dust outside the optically thick gas clumps, typically overestimates $f_{\rm esc}^{\rm LyC}$ (e.g., see also Gazagnes et al. 2020; Kakiichi & Gronke 2021). Accounting for this could potentially lower the $f_{\rm esc}^{\rm LyC}$ estimates presented in Pahl et al. (2021). However, we note that the $f_{\rm esc}^{\rm LyC} = (1-C_f^{\rm H\,I})$ approximation should be valid at the high $W_{\lambda}({\rm Ly}\,\alpha)$ values we are considering here, since these galaxies are generally expected to have low dust attenuation. Indeed, Saldana-Lopez et al. (2022a) conclude that this geometric consideration is insufficient to reconcile the $f_{\rm esc}^{\rm LyC}$ estimates.

Finally, it is clear that the choice of dust attenuation law can have a

strong systematic impact on the derived values of $f_{\rm esc}^{\rm LyC}$ (e.g., Begley et al. 2022). Indeed, Saldana-Lopez et al. (2022a) note that their $W_{\rm LIS}-f_{\rm esc}^{\rm LyC}$ calibration would predict $f_{\rm esc}^{\rm LyC}$ values that are higher by up to a factor 1.5, if they switch from the Reddy et al. (2016) dust attenuation law to a steeper SMC-like law (e.g., Gordon et al. 2003), which would be closer to the assumptions employed by Pahl et al. (2021) at high $W_{\lambda}({\rm Ly}\,\alpha)$. However, even in this case, the offset between the two estimates of $f_{\rm esc}^{\rm LyC}$ would still be a factor of \simeq 6. Ultimately, a combination of all of these different factors is likely

Ultimately, a combination of all of these different factors is likely to be having an impact. However, it is worth noting that, although the *absolute* $f_{\rm esc}^{\rm LyC}$ values are subject to potentially large systematic uncertainties, the *relative* values should be much less affected. Consequently, our conclusion that $f_{\rm esc}^{\rm Ly\alpha}$ and $f_{\rm esc}^{\rm LyC}$ are strongly correlated, and that the correlation is not driven by varying $W_{\lambda}({\rm Ly}\,\alpha)$, should still be robust, regardless of the exact normalization of either value.

6 SUMMARY

We have presented the results of a study exploring the connection between the Ly α escape fraction $(f_{\rm esc}^{\rm Ly}{}^{\alpha})$ and the Lyman continuum escape fraction $(f_{\rm esc}^{\rm Ly}{}^{C})$ for a sample of N=152 SFGs selected from the ESO VANDELS spectroscopic survey (McLure et al. 2018; Pentericci et al. 2018; Garilli et al. 2021) at $3.85 \le z_{\rm spec} \le 4.95$.

We combine measurements of $W_{\lambda}(\mathrm{Ly}\,\alpha)$ from ultra-deep, restframe FUV VANDELS spectra with H α equivalent widths derived from IRAC 3.6 μ m flux-excess measurements to estimate *individual* $f_{\mathrm{esc}}^{\mathrm{Ly}\alpha}$ values for our full sample. We also employ composites of the VANDELS spectra to investigate the FUV spectral features as a function of $f_{\mathrm{esc}}^{\mathrm{Ly}\alpha}$, controlling for variations in $W_{\lambda}(\mathrm{Ly}\,\alpha)$. From these composites, we measure the equivalent width of low-ionization-state ISM absorption features (W_{LIS}) to place constraints on $f_{\mathrm{esc}}^{\mathrm{LyC}}$ using a low-redshift $W_{\mathrm{LIS}}-f_{\mathrm{esc}}^{\mathrm{LyC}}$ calibration presented in Saldana-Lopez et al. (2022a). Our main results can be summarised as follows:

- (i) We find a positive correlation between $f_{\rm esc}^{\rm Ly\alpha}$ and $W_{\lambda}({\rm Ly}\,\alpha)$ ($\simeq 10\sigma$ significance), in which $f_{\rm esc}^{\rm Ly\alpha}$ monotonically increases from $f_{\rm esc}^{\rm Ly\alpha} \simeq 0.04$ at $W_{\lambda}({\rm Ly}\,\alpha) = 10$ Å to $f_{\rm esc}^{\rm Ly\alpha} \simeq 0.1$ at $W_{\lambda}({\rm Ly}\,\alpha) = 25$ Å. This represents the first measurement of the $f_{\rm esc}^{\rm Ly\alpha} W_{\lambda}({\rm Ly}\,\alpha)$ relation at z > 4 using *individual* $f_{\rm esc}^{\rm Ly\alpha}$ estimates.

 (ii) We show that the $f_{\rm esc}^{\rm Ly\alpha} W_{\lambda}({\rm Ly}\,\alpha)$ relation does not evolve strongly from z = 0 to z = 5, and that the correlation holds down to $W_{\lambda}({\rm Ly}\,\alpha) \simeq 0$ Å. Our results imply that the physical processes
- (ii) We show that the $f_{\rm esc}^{\rm Ly}\alpha W_{\lambda}({\rm Ly}\,\alpha)$ relation does not evolve strongly from z=0 to z=5, and that the correlation holds down to $W_{\lambda}({\rm Ly}\,\alpha) \simeq 0$ Å. Our results imply that the physical processes regulating the production and escape of ${\rm Ly}\,\alpha$ photons from low metallicity, high $\xi_{\rm ion}$ Ly α emitters do not change significantly across $\simeq 90$ per cent of cosmic history.
- (iii) Using composite spectra, we show that as $f_{\rm esc}^{{\rm Ly}\alpha}$ increases the strength of low-ionization-state ISM absorption lines decreases, consistent with a decrease in the covering fraction of neutral H_I gas.
- (iv) Using the relationship between the equivalent width of low-ionization absorption lines ($W_{\rm LIS}$) and $f_{\rm esc}^{\rm LyC}$ derived from low redshift galaxies in the LzLCS survey (Saldana-Lopez et al. 2022a), we find that $f_{\rm esc}^{\rm LyC} \simeq 0.15 f_{\rm esc}^{\rm Ly\alpha}$. Crucially, by constructing high- and low- $f_{\rm esc}^{\rm Ly\alpha}$ composite spectra with the same $W_{\lambda}({\rm Ly}\,\alpha)$, we demonstrate that the $f_{\rm esc}^{\rm LyC}-f_{\rm esc}^{\rm Ly\alpha}$ relation is not being driven by a secondary correlation between $f_{\rm esc}^{\rm Ly\alpha}$ and $W_{\lambda}({\rm Ly}\,\alpha)$.
- (v) We find that, at a given value of $W_{\lambda}(\text{Ly }\alpha)$, the absolute $f_{\text{esc}}^{\text{LyC}}$ values inferred from the low-redshift $W_{\text{LIS}} f_{\text{esc}}^{\text{LyC}}$ calibration are factor of ≥ 10 lower than recent direct measurements of $f_{\text{esc}}^{\text{LyC}}$ at

Donnan C. T., et al., 2022, MNRAS,

z > 3 (e.g., Steidel et al. 2018; Pahl et al. 2021; Begley et al. 2022). This is similar to the offset reported in Saldana-Lopez et al. (2022a). A number of systematic considerations may explain the discrepancy, but they remain to be fully understood. We argue that caution must therefore be used in inferring *absolute* values of $f_{\rm esc}^{\rm LyC}$ from $W_{\rm LIS}$ measurements at high-redshift.

In the future, JWST will offer improvements via direct spectroscopic and/or more accurate photometric H α measurements, which will lead to better constraints on $f_{\rm esc}^{{\rm Ly}\alpha}$ for larger numbers of individual galaxies.

ACKNOWLEDGEMENTS

R. Begley, R. J. McLure, J. S. Dunlop, D.J. McLeod, C. Donnan and M.L. Hamadouche acknowledge the support of the Science and Technology Facilities Council. F. Cullen and T. M. Stanton acknowledge the support from a UKRI Frontier Re- search Guarantee Grant [grant reference EP/X021025/1]. A. C. Carnall thanks the Leverhulme Trust for their support via a Lev- erhulme Early Career Fellowship. This research made use of Astropy, a community-developed core Python package for Astronomy (Astropy Collaboration et al. 2013, 2018), NumPy (Harris et al. 2020) and SciPy (Virtanen et al. 2020), Matplotlib (Hunter 2007), IPython (Pérez & Granger 2007) and NASA's Astrophysics Data System Bibliographic Services.

DATA AVAILABILITY

The VANDELS survey is a European Southern Observatory Public Spectroscopic Survey. The full spectroscopic dataset, together with the complementary photometric information and derived quantities are available from http://vandels.inaf.it, as well as from the ESO archive https://www.eso.org/qi/. For the purpose of open access, the author has applied a Creative Commons Attribution (CC BY) licence to any Author Accepted Manuscript version arising from this submission.

```
REFERENCES
Astropy Collaboration et al., 2013, A&A, 558, A33
Astropy Collaboration et al., 2018, AJ, 156, 123
Atek H., Kunth D., Hayes M., Östlin G., Mas-Hesse J. M., 2008, A&A, 488,
Begley R., et al., 2022, MNRAS, 513, 3510
Berry M., et al., 2012, ApJ, 749, 4
Bouwens R. J., et al., 2012, ApJ, 754, 83
Bouwens R. J., Smit R., Labbé I., Franx M., Caruana J., Oesch P., Stefanon
    M., Rasappu N., 2016, ApJ, 831, 176
Bruzual G., Charlot S., 2003, MNRAS, 344, 1000
Calzetti D., Armus L., Bohlin R. C., Kinney A. L., Koornneef J., Storchi-
    Bergmann T., 2000, ApJ, 533, 682
Cen R., Kimm T., 2015, ApJ, 801, L25
Chabrier G., 2003, PASP, 115, 763
Chary R., Petitjean P., Robertson B., Trenti M., Vangioni E., 2016, Space Sci.
    Rev., 202, 181
Chisholm J., et al., 2018, A&A, 616, A30
Cullen F., et al., 2018, MNRAS, 476, 3218
Cullen F., et al., 2019, MNRAS, 487, 2038
Cullen F., et al., 2020, MNRAS, 495, 1501
Cullen F., et al., 2021, MNRAS, 505, 903
Cullen F., et al., 2023, MNRAS, 520, 14
Dijkstra M., Gronke M., Venkatesan A., 2016, ApJ, 828, 71
```

```
Donnan C. T., McLeod D. J., McLure R. J., Dunlop J. S., Carnall A. C.,
    Cullen F., Magee D., 2023, MNRAS, 520, 4554
Du X., et al., 2018, ApJ, 860, 75
Duncan K., Conselice C. J., 2015, MNRAS, 451, 2030
Emami N., Siana B., Alavi A., Gburek T., Freeman W. R., Richard J., Weisz
    D. R., Stark D. P., 2020, ApJ, 895, 116
Erb D. K., Pettini M., Shapley A. E., Steidel C. C., Law D. R., Reddy N. A.,
    2010, ApJ, 719, 1168
Erb D. K., Pettini M., Steidel C. C., Strom A. L., Rudie G. C., Trainor R. F.,
    Shapley A. E., Reddy N. A., 2016, ApJ, 830, 52
Fan X., et al., 2006, AJ, 132, 117
Finkelstein S. L., et al., 2012, ApJ, 758, 93
Finkelstein S. L., et al., 2019, ApJ, 879, 36
Finkelstein S. L., et al., 2022, arXiv e-prints, p. arXiv:2211.05792
Flury S. R., et al., 2022a, ApJS, 260, 1
Flury S. R., et al., 2022b, ApJ, 930, 126
Galametz A., et al., 2013, ApJS, 206, 10
Garilli B., et al., 2021, A&A, 647, A150
Gazagnes S., Chisholm J., Schaerer D., Verhamme A., Izotov Y., 2020, A&A,
    639, A85
Gordon K. D., Clayton G. C., Misselt K. A., Landolt A. U., Wolff M. J., 2003,
    ApJ, 594, 279
Goto H., et al., 2021, ApJ, 923, 229
Grogin N. A., et al., 2011, ApJS, 197, 35
Guo Y., et al., 2013, The Astrophysical Journal Supplement Series, 207, 24
Harikane Y., et al., 2018, ApJ, 859, 84
Harikane Y., et al., 2022, arXiv e-prints, p. arXiv:2208.01612
Harris C. R., et al., 2020, Nature, 585, 357
Hayes M., Schaerer D., Östlin G., Mas-Hesse J. M., Atek H., Kunth D., 2011,
    ApJ, 730, 8
Hayes M., et al., 2013, ApJ, 765, L27
Henry A., Scarlata C., Martin C. L., Erb D., 2015, ApJ, 809, 19
Hunter J. D., 2007, Computing in Science & Engineering, 9, 90
Ishigaki M., Kawamata R., Ouchi M., Oguri M., Shimasaku K., Ono Y., 2018,
    ApJ, 854, 73
Iwata I., et al., 2022, MNRAS, 509, 1820
Izotov Y. I., Schaerer D., Worseck G., Verhamme A., Guseva N. G., Thuan
    T. X., Orlitová I., Fricke K. J., 2020, MNRAS, 491, 468
Jaskot A. E., Dowd T., Oey M. S., Scarlata C., McKinney J., 2019, ApJ, 885,
Kakiichi K., Gronke M., 2021, ApJ, 908, 30
Katz H., et al., 2022, MNRAS, 515, 4265
Kimm T., Blaizot J., Garel T., Michel-Dansac L., Katz H., Rosdahl J., Ver-
    hamme A., Haehnelt M., 2019, MNRAS, 486, 2215
Kimm T., Bieri R., Geen S., Rosdahl J., Blaizot J., Michel-Dansac L., Garel
    T., 2022, ApJS, 259, 21
Koekemoer A. M., et al., 2011, ApJS, 197, 36
Kornei K. A., Shapley A. E., Erb D. K., Steidel C. C., Reddy N. A., Pettini
    M., Bogosavljević M., 2010, ApJ, 711, 693
Kriek M., van Dokkum P. G., Labbé I., Franx M., Illingworth G. D., March-
    esini D., Quadri R. F., 2009, ApJ, 700, 221
Le Fèvre O., et al., 2003, in Iye M., Moorwood A. F. M., eds, Society of Photo-
    Optical Instrumentation Engineers (SPIE) Conference Series Vol. 4841,
    Instrument Design and Performance for Optical/Infrared Ground-based
    Telescopes. pp 1670–1681, doi:10.1117/12.460959
Madau P., Dickinson M., 2014, ARA&A, 52, 415
Maji M., et al., 2022, A&A, 663, A66
Marchi F., et al., 2018, A&A, 614, A11
Mármol-Queraltó E., McLure R. J., Cullen F., Dunlop J. S., Fontana A.,
    McLeod D. J., 2016, MNRAS, 460, 3587
Mason C. A., et al., 2019, MNRAS, 485, 3947
Matsuoka Y., et al., 2023, arXiv e-prints, p. arXiv:2305.11225
Matthee J., Sobral D., Oteo I., Best P., Smail I., Röttgering H., Paulino-Afonso
    A., 2016, MNRAS, 458, 449
McGreer I. D., Mesinger A., D'Odorico V., 2015, MNRAS, 447, 499
McLeod D. J., et al., 2023, arXiv e-prints, p. arXiv:2304.14469
McLure R. J., et al., 2018, MNRAS, 479, 25
```

- 12 R. Begley et al. Meštrić U., Ryan-Weber E. V., Cooke J., Bassett R., Prichard L. J., Rafelski M., 2021, MNRAS, Naidu R. P., Tacchella S., Mason C. A., Bose S., Oesch P. A., Conroy C., 2020, ApJ, 892, 109 Nakajima K., Ellis R. S., Robertson B. E., Tang M., Stark D. P., 2020, ApJ, 889, 161 Oesch P. A., Bouwens R. J., Illingworth G. D., Labbé I., Stefanon M., 2018, ApJ, 855, 105 Oke J. B., Gunn J. E., 1983, ApJ, 266, 713 Osterbrock D. E., 1989, Astrophysics of gaseous nebulae and active galactic Pahl A. J., Shapley A., Steidel C. C., Chen Y., Reddy N. A., 2021, MNRAS, 505, 2447 Pentericci L., et al., 2018, A&A, 616, A174 Pérez F., Granger B. E., 2007, Computing in Science and Engineering, 9, 21 Pucha R., Reddy N. A., Dey A., Juneau S., Lee K.-S., Prescott M. K. M., Shivaei I., Hong S., 2022, AJ, 164, 159 Reddy N. A., Steidel C. C., Pettini M., Bogosavljević M., Shapley A. E., 2016, ApJ, 828, 108 Reddy N. A., et al., 2018, ApJ, 853, 56 Reddy N. A., et al., 2020, ApJ, 902, 123 Robertson B. E., 2021, arXiv e-prints, p. arXiv:2110.13160 Robertson B. E., Ellis R. S., Dunlop J. S., McLure R. J., Stark D. P., 2010, Nature, 468, 49 Robertson B. E., Ellis R. S., Furlanetto S. R., Dunlop J. S., 2015, ApJ, 802, T.19 Rosdahl J., et al., 2018, MNRAS, 479, 994 Saldana-Lopez A., et al., 2022a, arXiv e-prints, p. arXiv:2211.01351 Saldana-Lopez A., et al., 2022b, A&A, 663, A59 Schaerer D., et al., 2022, A&A, 658, L11 Schreiber C., et al., 2018, A&A, 611, A22 Shapley A. E., Steidel C. C., Pettini M., Adelberger K. L., 2003, ApJ, 588, 65 Shim H., Chary R.-R., Dickinson M., Lin L., Spinrad H., Stern D., Yan C.-H., 2011, ApJ, 738, 69 Smit R., Bouwens R. J., Labbé I., Franx M., Wilkins S. M., Oesch P. A., 2016, ApJ, 833, 254 Sobral D., Matthee J., 2019, A&A, 623, A157 Sobral D., et al., 2017, MNRAS, 466, 1242 Speagle J. S., 2020, MNRAS, 493, 3132 Stark D. P., Schenker M. A., Ellis R., Robertson B., McLure R., Dunlop J., 2013, ApJ, 763, 129 Stark D. P., et al., 2015, MNRAS, 454, 1393 Steidel C. C., Bogosavljević M., Shapley A. E., Reddy N. A., Rudie G. C., Pettini M., Trainor R. F., Strom A. L., 2018, ApJ, 869, 123 Trainor R. F., Steidel C. C., Strom A. L., Rudie G. C., 2015, ApJ, 809, 89 Trainor R. F., Strom A. L., Steidel C. C., Rudie G. C., 2016, ApJ, 832, 171 Trainor R. F., Strom A. L., Steidel C. C., Rudie G. C., Chen Y., Theios R. L.,
- 2019, ApJ, 887, 85 Vanzella E., et al., 2016, ApJ, 825, 41

Verhamme A., Orlitová I., Schaerer D., Hayes M., 2015, A&A, 578, A7

Verhamme A., Orlitová I., Schaerer D., Izotov Y., Worseck G., Thuan T. X., Guseva N., 2017, A&A, 597, A13

Virtanen P., et al., 2020, Nature Methods, 17, 261

Wang B., Heckman T. M., Leitherer C., Alexandroff R., Borthakur S., Overzier R. A., 2019, ApJ, 885, 57

Wise J. H., Demchenko V. G., Halicek M. T., Norman M. L., Turk M. J., Abel T., Smith B. D., 2014, MNRAS, 442, 2560

Wuyts S., et al., 2013, ApJ, 779, 135

Yang H., et al., 2017, ApJ, 844, 171

This paper has been typeset from a T_EX/L^2T_EX file prepared by the author.